Nanoscale

PAPER

View Article Online
View Journal | View Issue

Cite this: *Nanoscale*, 2023, **15**, 18891

Sudden collective atomic rearrangements trigger the growth of defect-free silver icosahedra†

Diana Nelli, [a] Cesare Roncaglia, [a] Riccardo Ferrando, *[a] Zeinab Kataya, [b] Yves Garreau, [c,d] Alessandro Coati, [c] Caroline Andreazza-Vignolle [b] and Pascal Andreazza *[b]

Received 8th September 2023,
Accepted 31st October 2023

DOI: 10.1039/d3nr04530g

rsc.li/nanoscale

The growth of Ag clusters on amorphous carbon substrates is studied *in situ* by X-ray scattering experiments, whose final outcome is imaged by electron microscopy. The real-time analysis of the growth process at room temperature shows the formation of a large majority of icosahedral structures by a shell-by-shell growth mode which produces smooth and nearly defect-free structures. Molecular dynamics simulations supported by *ab initio* calculations reveal that the shell-by-shell mode is possible because of the occurrence of collective displacements which involve the concerted motion of many atoms of the growing shell. These collective processes are a kind of *black swan* event, as they occur suddenly and rarely, but their occurrence is decisive for the final outcome of the growth. Annealing and ageing experiments show that the as-grown icosahedra are metastable, in agreement with the energetic stability calculations.

1. Introduction

An important issue in the growth of materials is the achievement of regular and smooth shapes. In the case of thin films, smooth structures can be obtained by layer-by-layer (LBL) growth, in which an atomic layer is mostly complete before a new one starts to grow on top of it. The conditions allowing LBL growth have been deeply studied and understood.[1] Obtaining such regular growth for nanoscale objects, such as nanoparticles,[2–5] introduces new challenges. In fact nanoparticles present inequivalent adsorption sites (*e.g.* at edges and vertices) even when they are free of defects, and their growth is a fully three-dimensional phenomenon in which both the structure and symmetry can dynamically change.[6–8] The equivalent of LBL growth for nanoparticles is shell-by-shell (SBS) growth,[9–11] whose aim is not only to form regular and smooth shapes, but also to preserve the initial structural motif which acts as a template. In this respect, the growth of icosahedra is a paradigmatic example, since icosahedra are shell structures *par excellence*.[12–14]

In thin films, LBL growth is obtained when there is effective mobility between the different growing layers (*inter-layer* mobility),[15] which, in the most widely accepted scenario, is ensured by the surface diffusion of individual adatoms.[1] Contributions from multi-atom processes are also invoked, but they are in most cases exchange processes involving a few atoms or concerted displacements of small islands on the otherwise flat surface.[16,17] In order to ensure inter-layer mobility, a deposited atom must be able to diffuse on a flat terrace, in order to reach its border. Then, the atom must be able to cross the border to descend to the lower level. This is often the rate-limiting step for LBL growth, because step descent presents in most cases an additional contribution to the energy barrier compared to terrace diffusion. This additional contribution is known as the Ehrlich–Schwoebel (ES) barrier.[18,19] In nanoparticles, the growth process is more complex since the presence of surface strain,[20] of edges and vertices make the growing shell prone to defects, that hinder the perfect SBS growth and must be eliminated before the completion of the growing shell.

Here we study the growth of silver clusters both experimentally and using computer simulations. The experimental observations combine grazing incidence X-ray scattering at wide and small angles (GIWAXS and GISAXS, respectively), which allow the real-time analysis of very large samples of growing clusters, and High Resolution Transmission Electron Microscopy (HRTEM) imaging of the final growth outcomes

[a]*Dipartimento di Fisica, Università di Genova, Via Dodecaneso 33, 16146 Genova, Italy. E-mail: ferrando@fisica.unige.it*
[b]*Université d'Orléans, CNRS, ICMN UMR7374, 1b rue de la Férollerie, F-45071 Orléans, France. E-mail: pascal.andreazza@univ-orleans.fr*
[c]*Synchrotron Soleil, L'Orme de Merisiers, F-91192 Gif-sur-Yvette, France*
[d]*Université de Paris, CNRS, Laboratoire Matériaux et Phénomènes Quantiques UMR7162, F-75013 Paris, France*

†Electronic supplementary information (ESI) available. See DOI: https://doi.org/10.1039/d3nr04530g

with atomic resolution. The calculations include molecular dynamics (MD) simulations which allow following of the growth mechanism atom by atom, complemented by Density Functional Theory (DFT) calculations to support the accuracy of the results.

Our experiments show the formation of almost perfect Mackay icosahedra[21] which takes place in an SBS mode. This type of SBS growth is made possible by the occurrence of *intralayer* rearrangement processes, which do not occur through the diffusion of individual adatoms on the surface, but through complex collective displacements of many atoms at the same time. These concerted processes are a kind of *black swan* event, as they occur very rarely during the growth process, but their occurrence is crucial to make the SBS mode possible. Our simulations therefore show that SBS growth is made possible by other crucial processes beyond interlayer mobility as limited by the ES barrier. In addition, we demonstrate that the as-grown icosahedra are metastable structures, which transform into decahedral shapes upon annealing and/or ageing.

2. Methods

2.1. Experimental methods

Ag metal nanoparticles were prepared at room temperature (RT) by UHV vapor deposition on thermally oxidized Si(100) wafers covered by an amorphous carbon layer or on an amorphous carbon membrane self-supported on TEM Cu grids.[22,23] Nanoparticle surfaces can be considered bare, apart from the interface with the substrates, which were chosen to limit the cluster substrate interactions and to allow comparisons between X-ray scattering and TEM measurements.[24] The amorphous carbon structure and the interface energy between carbon and Ag induce the formation of a randomly oriented assembly of isolated particles without a preferential crystallographic orientation. Substrates were degassed at 500 K with a ramp rate of 2 K mn^{-1} to clean the carbon layer (*i.e.* to vaporize water and some organic species). The metal vapor was obtained using an Omicron type evaporator at an initial pressure of 1×10^{-10} mbar and an operating pressure of 2×10^{-10} mbar during deposition. The deposition rate was controlled using an *in situ* flux monitor, calibrated *in situ* using a quartz microbalance and *ex situ* by Rutherford Backscattering Spectroscopy (RBS), in order to determine the deposition rate and the quantity of the deposited Ag atoms. The deduced deposition rates were in the range of 0.25×10^{15} atoms per cm^2 per h. Transmission Electron Microscopy (TEM) and grazing incidence X-ray scattering at wide and small angles (GIWAXS and GISAXS[24,25]) were both performed to determine the NP structure and morphology, respectively. High Resolution TEM (HRTEM) was performed, using a double aberration-corrected JEOL ACCELARL200 Cold FEG microscope, to investigate the proportion of Ih, Dh and TO structures in the samples. Since the HRTEM images are dependent on the defocus and aberration coefficients, in order to quantitatively analyze these images, "Dr Probe" software simulations of HRTEM images were performed[26] under various TEM conditions and for various structures and sizes. *In situ* Grazing Incidence Small Angle X-ray Scattering (GISAXS) and Grazing Incidence Wide Angle X-ray Scattering (GIWAXS) measurements were carried out at a photon energy of 7.7 keV on the SIXS beamline[27,28] at the SOLEIL Synchrotron in Gif-sur-Yvette, France. The scattered intensities for GISAXS and GIWAXS were recorded independently and simultaneously during the formation of supported Ag clusters or during their ageing at a temperature under an ultra-high vacuum. For GIWAXS data analysis: the 1D experimental scattering profile was compared with calculated patterns obtained from simulated cluster models on the basis of the Debye equation[22,25] and considering the set-up geometry, from dedicated home-made software.[29] A weighted sum of the intensities from several sizes and/or structures was used to fit GIWAXS patterns considering the size distribution coming independently from GISAXS results obtained *in situ* and simultaneously and checked where possible by HRTEM observation.[23,28]

2.2. Molecular dynamics simulations

Growth simulations are made with MD using the same type of procedure adopted in ref. 7. Simulations start from an icosahedral structure of 147 atoms on which atoms are deposited one by one isotropically from random directions. The deposition rate is 1 atom every 10 ns. Simulations are stopped when a size of 561 is reached. The equations of motion are solved using the Velocity Verlet algorithm with a time step of 5 fs. Temperature is kept constant using an Andersen thermostat. For each temperature (300, 400 and 500 K), 5 independent simulations are made. Annealing simulations are made by evolving the clusters at constant size and temperature. Temperatures are chosen in the range 500–700 K.

2.3. DFT calculations

All DFT calculations reported in Table 1 were made with open-source QUANTUM ESPRESSO software,[30] using three different exchange–correlation functionals: Perdew–Burke–Ernzerhof (PBE),[31] an improved version of PBE for solids (PBEsol)[32] and the Local Density Approximation (LDA).[33] The convergence thresholds for the total energy, total force, and electronic calculations were set to 10^{-4} Ry, 10^{-3} Ry $a.u.^{-1}$ and 5×10^{-6} Ry, respectively. We used a periodic cubic cell, whose size was always set to 30 Å. Cutoffs for wavefunction and charge density were set to 45 and 181 Ry, respectively, for all three func-

Table 1 Gupta and DFT values for the energy difference ΔE (in eV) between islands on anti-Macky and Mackay stacking. The corresponding configurations are given in Fig. S2, ESI†

	$N = 153$	$N = 159$	$N = 165$	$N = 171$
Gupta	−0.326	−0.650	−0.747	0.065
PBE	−0.512	−0.545	−0.291	0.179
LDA	−0.679	−0.796	−0.574	0.231
PBEsol	−0.583	−0.690	−0.451	0.229

tionals. In particular we used the following pseudopotentials: Ag.pbe-n-kjpaw_psl.1.0.0.UPF, Ag.pbesol-n-kjpaw_psl.1.0.0.UPF and Ag.pz-n-kjpaw_psl.1.0.0.UPF for PBE, PBEsol and LDA, respectively. They are currently available at **https://pseudopotentials.quantum-espresso.org/legacy_tables/ps-library/ag**.

3. Results

3.1. Room temperature growth – Experimental data

Ag metal nanoparticles were prepared at room temperature (RT) by UHV vapor deposition on thermally oxidized Si(100) wafers covered with an amorphous carbon layer or on an amorphous carbon membrane self-supported on TEM Cu grids (see the Methods section for details). Several samples were investigated to reveal the structural evolution with time at different activation temperatures (from room temperature (RT) to 600 K) and to check the experimental result reproducibility. First of all, the growth of Ag clusters obtained in the Volmer–Weber vapor condensation mode[24,34] was followed by X-ray scattering from nucleation to final growth in the range of some tens of atoms to D = 2.5 nm in diameter. Fig. 1(a) shows real-time monitoring of the structure of clusters under ultra-high vacuum during deposition at 300 K, in a short acquisition time to simultaneously measure the scattered intensity at small and large angles, with a set of spectra collected for every deposition of 15 atoms on average per cluster. The comparison with GIWAXS spectra simulations (Fig. 1(b)) reveals that the icosahedral (Ih) structure of the cluster is the main structure from an ultra-small size (D = 1.5 nm) to a larger size (D = 2.5 nm) with the size distribution ($\sigma(D)/D$ = 0.3) measured by GISAXS and in agreement with TEM observations. Note that an unambiguous determination of the structure for Ag clusters below 1–1.5 nm is not feasible by X-ray scattering analysis, because of the dominance of surface disordering at a small size.[35] We note that our results agree with the X-ray scattering measurement performed on Ag particles obtained by vapor deposition in ref. 28, which reveals the stability of the Ih structure during the growth of particles at RT with an increase in size from 1 to 3 nm. Note also that decahedral (Dh) and fcc truncated octahedral (TO) structures would not fit the spectra well (see Fig. S1, ESI†). Fig. 2 shows the HRTEM images of a similar sample illustrating the structure and size distribution of Ag supported nanoparticles (NPs) prepared at 300 K up to an average diameter of 2.5 nm. The samples shown in Fig. 2 were observed just after the end of NP formation (*i.e.* several tens of minutes) by keeping the samples at RT. Fig. 2(a) shows a low magnification HRTEM image of Ag NPs, while Fig. 2(b–d) show high magnification images of selected NPs in the Ih structural configuration, which is the major structure under these conditions. The associated simulated HRTEM images in the two-fold symmetry zone axis (Fig. 2(f)) and three-fold zone axis (Fig. 2(e)) correspond to the same orientations, structures of clusters and the same observation conditions as the experimental images of Fig. 2(b, d) and (c), respectively. In summary, both the real-time X-ray data and the HRTEM characterization

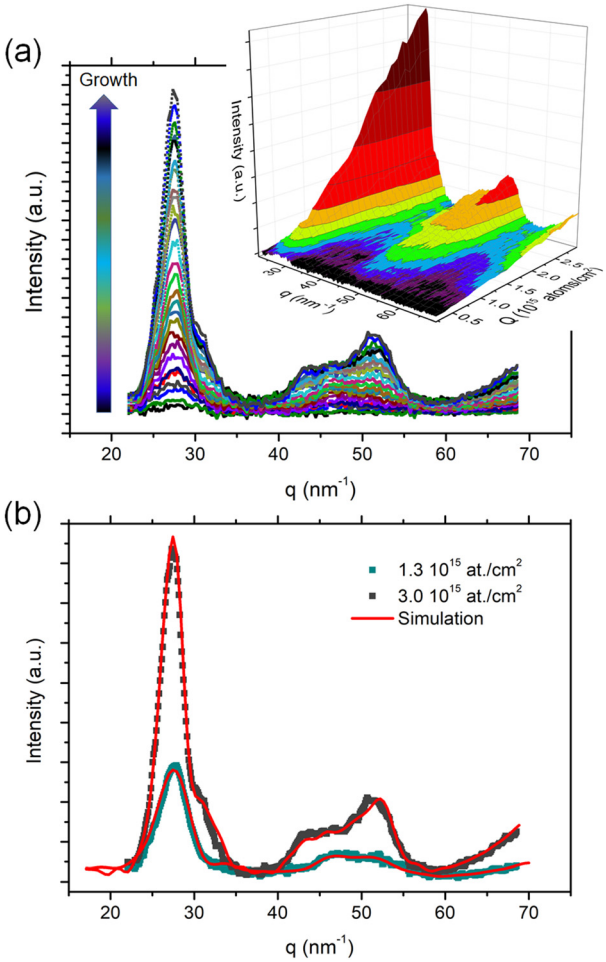

Fig. 1 (a) GIWAXS experimental spectrum of Ag nanoparticle assembly during the growth of 0.20 to 3.00 × 10^{15} deposited Ag atoms per cm^2 which corresponds to clusters from several tens to about 500 atoms, with a step of data collection of 15 atoms per cluster at each spectrum. In the inset 3D graph, (b) two representative GIWAXS experimental spectra obtained during deposition (dots); with calculated spectra (red line) in good agreement with experiments corresponding to a distribution of Ih structure models after energy minimization using MC simulations: for 1.3 × 10^{15} Ag atoms per cm^2 (about 1.5 nm size) from Ag_{55} to Ag_{309} models were used while for 3.0 × 10^{15} Ag atoms per cm^2 (about 2.5 nm size) from Ag_{309} to Ag_{923} models.

of the final NPs clearly indicate that growth at RT is dominated by icosahedral structures in the diameter range from 1 to 3 nm, corresponding to clusters containing ~100 to a few hundred atoms. The diameters of the ideal icosahedra of 147, 309 and 561 atoms fall in this range. We also note that the clusters shown in Fig. 2(b–d) have an almost perfect icosahedral shape, which very nicely agrees with the simulated HRTEM images of the ideal icosahedra of Fig. 2(e and f).

3.2. Unravelling the growth mechanisms using MD simulations

In our growth simulations we start from the perfect Ih of size 147, which is in the low-size limit of the clusters observed in

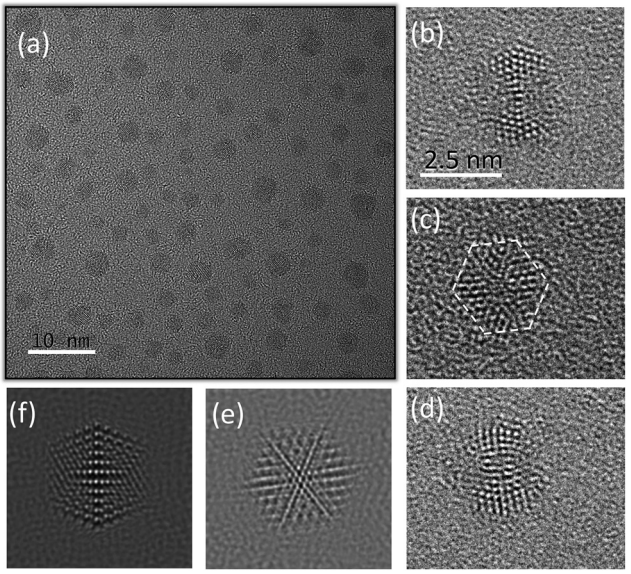

Fig. 2 HRTEM images obtained on Ag NPs just after deposition: (a) in a large area; (b)–(d) at a high magnification with associated Ih simulated HRTEM images; (f) in a two-fold symmetry zone axis corresponding to (b) and (d) clusters and (e) in a three-fold zone axis corresponding to the (c) cluster.

our experiments. The simulations are made in a vacuum without any substrate. This choice, which allows the extension of the time scale, is justified by the fact that this type of substrate has been shown to have quite small effects on the growth pathways of Ag–Co nanoalloys, which produce the same structural motifs as in a vacuum.[28,36] In Fig. 3(a1)–(a3) we show snapshots from representative growth simulations at T = 300, 400 and 500 K, taken at magic sizes of 309 and 561, *i.e.* after depositing 162 and 414 atoms, respectively. For every temperature, the clusters keep growing within the Ih motif. Moreover, we note that, even in the limited time scale of our MD simulations of ~5 μs, the growth produces quite smooth structures which replicate well the original Ih template. At 500 K, nearly perfect icosahedra are observed at magic sizes; at size 561, the second shell is almost complete in all simulations, with just 1–3 atoms on the third shell. At lower temperatures, more atoms are missing from the second shell (8–29 at 400 K and 18–38 at 300 K), which is however very regular and quite close to completion (88–96% at 400 K and 85–93% at 300 K).

In order to better quantify the shell-by-shell character of the template growth of icosahedra, we calculate the number of atoms in the shells as the growth proceeds. The results for the three different growth temperatures are shown in Fig. 3(b1)–(b3). Panels (c1), (c2), and (c3) report a magnification of the initial stages of growth. Growth is reasonably shell-by-shell even at 300 K, since the third growing shell begins to form when the first growing shell is already fully complete and the second growing shell contains about 170 atoms on a total of 252. At 400 K the shell-by-shell growth is already almost perfect, and at 500 K it essentially matches the ideal behaviour.

The smoothness of the shell-by-shell growth observed in our MD simulations indicates that the inter-layer mobility of Ag atoms is activated. This behaviour might be expected, as ES barriers for descending steps on (111) surfaces are low in Ag.[37] However, as we will see in the following, the descent of Ag atoms at steps is not the only factor for achieving smooth shell-by-shell growth. Other phenomena are even more important. We remark that the good quality of the final outcomes of MD simulations and of the experimentally observed icosahedra are in perfect agreement. We recall that the time scale of MD simulations is much shorter compared to the time scale of the growth experiments; therefore, in light of our very good simulation results, it is not surprising that no defective or amorphous structures have been observed in the experiments, in which Ag clusters have much more time to rearrange and to eliminate defects than in simulations. In addition, we note that the time scale of our simulations is sufficient to overcome the rate-limiting step for smooth and regular icosahedral growth; we expect that longer simulation times would not introduce significant changes or improvements.

A closer inspection of the initial stages of the growth allows us to single out the occurrence of peculiar growth mechanisms. The non-zero values of the yellow line in Fig. 3(c1) indicate that a few atoms remain in the second growing shell for some time, and then they descend down to the first growing shell. This presence of a few atoms in the second shell is due to the formation of an anti-Mackay cap (see Fig. 4(a)) in the first shell. Anti-Mackay islands are placed on hcp positions on top of the fcc tetrahedra that form the icosahedron.[38] These triangular faulted islands are energetically favourable on the facets of the icosahedron because on these facets there are more hcp than fcc adsorption sites.[39] When two triangular islands are formed on adjacent facets, they create fourfold sites in between which may act as trapping sites for newly deposited atoms in the second shell (as in Fig. 4(b)), especially at 300 K. We have studied the adsorption of one Ag atom on three-fold and four-fold sites above the anti-Mackay island, and we have found that four-fold sites are lower in energy by 0.35 eV. This means that Ag atoms have to cross an additional barrier of 0.35 eV for diffusing from four-fold to three-fold sites, which is considerably larger than the additional ES barrier for step descent, which can be lower than 0.2 eV.[37] Therefore, the rate-limiting step for a smooth shell-by-shell icosahedral growth is not the ES barrier at step borders, but it would be the escape from the four-fold sites of the anti-Mackay islands that are formed during the growth. As we shall see in the following, the arising picture is indeed more complex.

The formation of an incomplete anti-Mackay shell is observed in all simulations. Anti-Mackay stacking is energetically favourable over the Mackay stacking only when the shell is largely incomplete. This point has been verified by calculating the energy difference ΔE between configurations with anti-Mackay and Mackay islands of different sizes, both using the Gupta potential and Density Functional Theory (DFT), with three different exchange–correlation functionals: PBE,[31] LDA[33] and

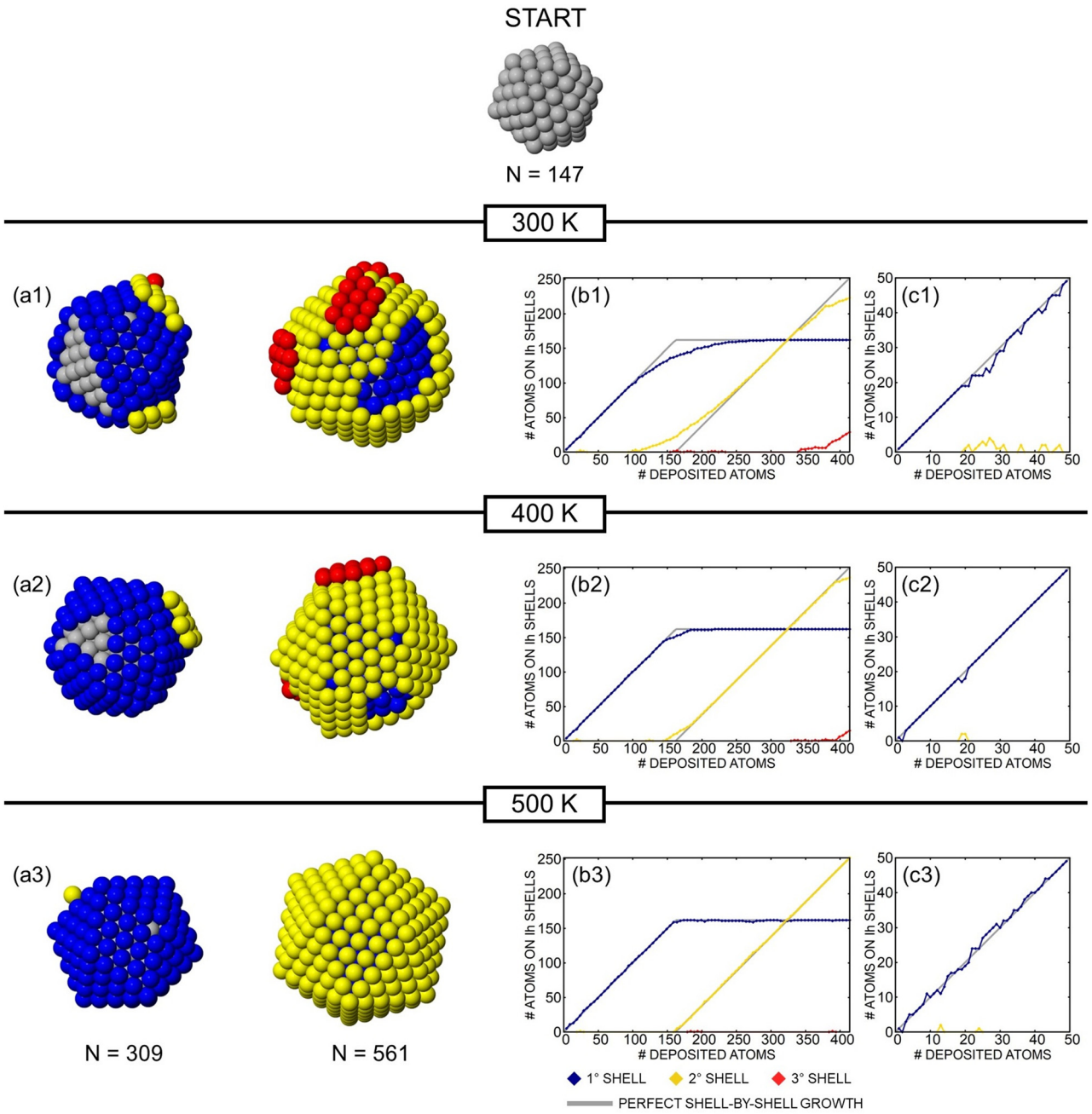

Fig. 3 Results from simulations at different temperatures. The snapshots in (a1), (a2) and (a3) are taken at icosahedral magic numbers (N = 309 and N = 561). Atoms belonging to the original 147-atoms Ih are coloured in grey; atoms in the first, second and third growing shells are coloured in blue, yellow and red, respectively. (b1)–(b3) Number of atoms in the first, second and third growing shells during the simulation, as a function of the number of deposited atoms. The behaviour of a perfect shell-by-shell growth is shown for comparison. In c1, c2 and c3 we show the first steps of the growth of the first shell.

PBEsol[32] (more details about DFT calculations can be found in section 3). The results are reported in Table 1. All calculations very well agree in predicting that anti-Mackay islands are favourable up to size 165 (18 deposited atoms), and that the Mackay stacking becomes energetically favorable between sizes 165 and 171. This change in energetic stability is the driving force of the anti-Mackay to the Mackay arrangement which is always observed well before the completion of the shell.

Now we closely look at the transition anti-Mackay → Mackay (aM → M) transformation. In Fig. 5 we report some snapshots from a simulation at 300 K. We note that the size and the shape of the growing shell at which the transformation occurs is different in all simulations. At 300 K, the size of the transforming shell is between 26 atoms (as in Fig. 5) and 89 atoms, and it is therefore larger than the size at which the stability reversal between the anti-Mackay and the Mackay arrangement

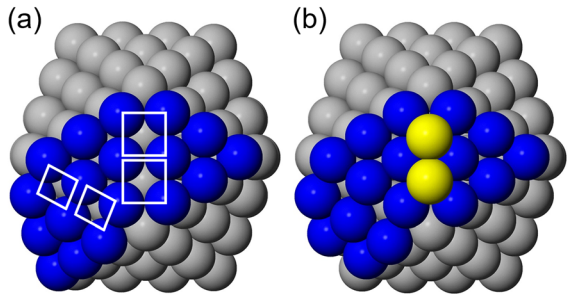

Fig. 4 Anti-Mackay incomplete first shell. (a) The shell is formed by three complete triangular islands on hcp stacking. The white squares enclose the fourfold adsorption sites. In (b) two atoms are adsorbed on these fourfold sites, thus belonging to the second growing layer.

is expected (*i.e.* between 18 and 24 atoms according to Table 1). aM → M transformation occurs at smaller and smaller sizes with an increase in temperature. A rich variety of transformation pathways can be collected. However, the pathways share some common features, that we describe with the help of Fig. 5.

In Fig. 5(a), the anti-Mackay shell is made of three complete triangular islands (in red, yellow and blue), an incomplete island (orange), one adatom in an hcp site (white) and two more atoms on the edge (green). At variance with yellow atoms in Fig. 4(b), the two green atoms belong to the first shell, as they are the first neighbours of some atoms of the initial seed. These atoms were initially in the second shell (as in Fig. 4(b)) and then they sank down to the first shell, slightly distorting the perfect anti-Mackay pattern. This is frequently observed in simulations at 300 K. We note that the presence of atoms in such a configuration is not necessary for the aM → M transformation. However, the transformation is never observed when some atoms are placed on fourfold sites as in Fig. 4(b); in order to make the transformation possible, those atoms must either sink down to the position of Fig. 5(a) or leave the fourfold sites to accommodate elsewhere. In Fig. 5(b) we show the first intermediate configuration of the aM → M transformation. This corresponds to a very shallow local energy minimum, which is very quickly crossed, in 1–2 ps. We have however verified that b is a true local minimum with real vibrational frequencies. In this configuration, the green atoms have moved closer to the vertex, which now has six first neighbours on the surface. At the same time, the red and the orange islands are further shifted away from the anti-Mackay sites. The white atom has become highly compressed, and quickly moves to a nearby site, as in Fig. 5(c). The lifetime of (c) is a little longer, of the order of tens of ps. Atoms around the fivefold vertex now form an open pentagon. In the (c) → (d) transition, the pentagon is closed and becomes regular, due to the displacement of all atoms in the shell, which perform a kind of concerted rotation around the vertex. In this configuration, Mackay stacking is achieved. The energy in (d) is lower than in (c), and also slightly lower than in (a). From this point on, growth continues within the Mackay stacking, as the newly deposited atoms attach to the Mackay growing shell and reinforce its stability. In the growth of the second shell we observe the same type of aM → M transformation. In this case, the evolution pathways are even more complicated, as disconnected anti-Mackay patches can form in different parts of the shell, which may transform to Mackay independently.

To demonstrate that the aM → M transformation shown in Fig. 5(c and d) is indeed due to a single collective process, we compare the timescale of such a process (of the order of a few picoseconds) with the typical time that one Ag atom with thermal velocity would take to cross a nearest-neighbour distance (2.89 Å), which is 2 ps at 300 K. This means that the transitions shown in Fig. 5, and especially the transition from (c) to (d), are sudden and collective, because separate and con-

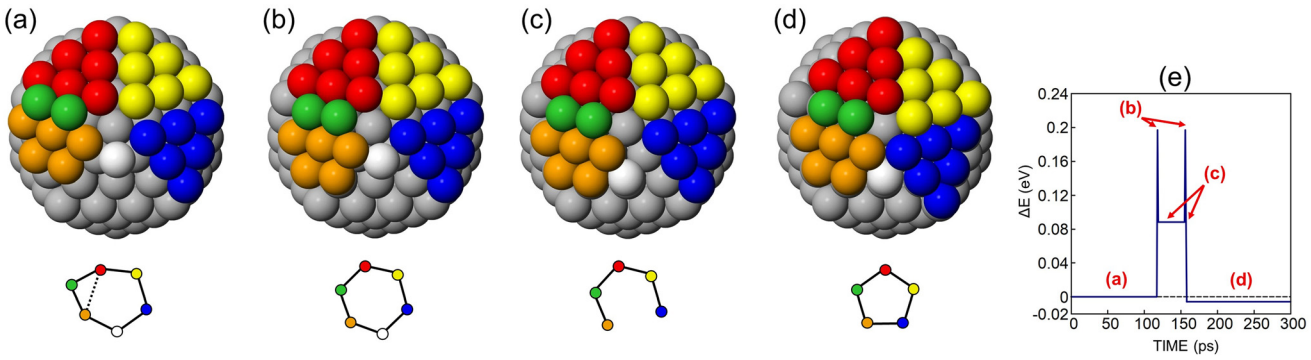

Fig. 5 Configurations of the local minima visited during a representative aM → M transformation of an incomplete shell. In (a) the anti-Mackay shell is formed by three complete triangular islands (red, yellow and blue), plus an incomplete island (orange), one adatom in an hcp site (white) and two more atoms at the edge (green). (b) and (c) Intermediate configurations of the transformation. (d) The shell in Mackay stacking. Under each configuration, we show the atoms of the first shell that surround the vertex of the 147-atom icosahedral seed. In (e) we show the evolution of the potential energy after local minimization, taking a snapshot every picosecond. The zero level of the energy is that of configuration (a). The evolution of the potential energy shows that the cluster explores only four local minima with the sequence (a) → (b) → (c) → (b) → (c) → (d). We note that configurations in (c) and (d) are separated by 1 ps in the simulation, and therefore the transformation can be only of collective character since there are no local minima visited in between.

secutive diffusion processes of so many individual atoms would take much longer times. Therefore, the transition from (c) to (d) corresponds to the crossing of a single saddle point separating two adjacent local minima. The crossing of that saddle point corresponds to the collective displacement of many atoms altogether.

We note that the experimental detection of aM → M transformation is extremely challenging due to the small differences between the two icosahedral configurations. Specifically, the transformation cannot be detected by the X-ray scattering technique employed here, as we discuss in the ESI.† In fact, the simulated GIWAXS spectra of 165-atom anti-Mackay and Mackay icosahedra are hardly distinguishable (see Fig. S3, ESI†), and the small differences are expected to be blurred by size-distribution effects in the nanoparticle sample.

In summary, our simulations show that the rearrangement of atomic shells is not due to the displacement of individual atoms which change their position by surface diffusion. Instead, atomic shells rearrange by collective processes where many atoms move at the same time in a concerted way. Collective processes are already observed even on the time scale of our simulations. Therefore we expect that, in general, they can play an essential role in the growth and structural rearrangement of metallic nanoparticles in the solid state.

3.3. Ageing, annealing and transition to equilibrium

After determining that Ag clusters grow within the icosahedral motif, we investigate whether these structures are to be considered at thermodynamic equilibrium or not. To this end, we perform two types of observations: after ageing of the clusters in Fig. 1 and 2 for 24 h under UHV conditions at RT and after annealing by increasing the temperature up to 600 K of a population grown at RT. Examples of the structures after 24 h of ageing at RT are given in Fig. 6. Two Dh cluster orientations are shown in Fig. 6(a), (c) and (b), with the associated simulated HRTEM images in Fig. 6(f) and (e), respectively. These images correspond to the Dh structural configuration observed in a larger proportion in the sample 24 h after the deposition. An interesting image is shown in Fig. 6(d), with a cluster which cannot be classified either as Ih or as Dh. This could be an intermediate stage of the transformation from the Ih to the Dh structure, which is complete for the great majority of the clusters. We remark that the discrimination of the cluster structure by the HRTEM observation may strongly depend on the orientation of clusters with respect to the electron beam. Consequently, a precise quantitative determination of Dh *vs.* Ih cluster proportion can be difficult. On the other hand, X-ray scattering measurements on a large area are less dependent on the cluster orientation on the substrate than HRTEM observations, and allow the collection of richer statistics, on samples of $\sim 10^{10}$ clusters in the analyzed area, without any risk of excluding parts of the cluster population. Thus, as in the measurement corresponding to Fig. 1, the structural distribution was also investigated by *in situ* X-ray scattering under UHV conditions on another sample during deposition at 300 K and during ageing activation with an increase in the temperature of up to 600 K. Fig. 7 reveals that at 300 K, just during the growth process, the distribution is centered at 2–2.5 nm in size, with a clear majority of Ih structures (about 90%), essentially the same as in Fig. 1. After thermal activation, the Ih proportion decreases to 50% to the benefit of Dh structures in the same size range. We note that the metastable character of icosahedra is compatible with recent results on Ag clusters of sizes around 309 grown in the gas phase.[40] We note that the change in the particle size distribution from the end of the growth at 300 K to the progressive annealing at 600 K is very small. This reveals that both Ostwald ripening and cluster diffusion leading to coalescence are very limited during this process. Therefore, the annealing process leads mainly to an accelerated thermal ageing of the initial clusters.

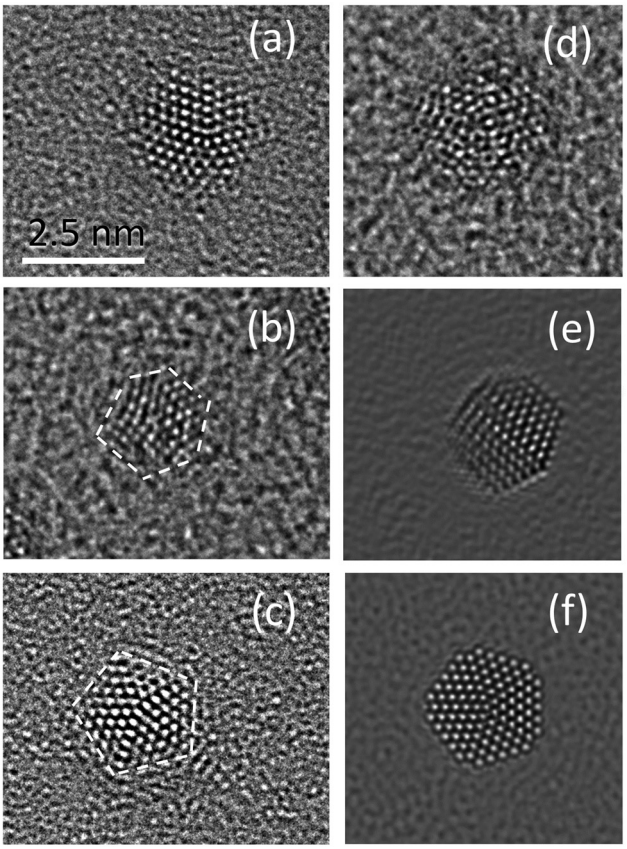

Fig. 6 (a–d) HRTEM images obtained on Ag NPs after 24 h of ageing in an UHV at 300 K. (a), (b), and (c) Dh structures, and (d) an intermediate structure between Ih and Dh. (e) and (f) Dh simulated HRTEM images with a five-fold-axis: (e) in the plane and (f) perpendicular to the image plane. These images have been obtained from MD simulated models using "Dr Probe" software.[26] These simulated images very well correspond to the real clusters in (b) and (c).

The results of the ageing/annealing experiments are compared with the theoretical predictions reported in Fig. 8, in which we report the excess energy

$$E_{\mathrm{exc}} = \frac{E - N\varepsilon_{\mathrm{b}}}{N^{2/3}}, \qquad (1)$$

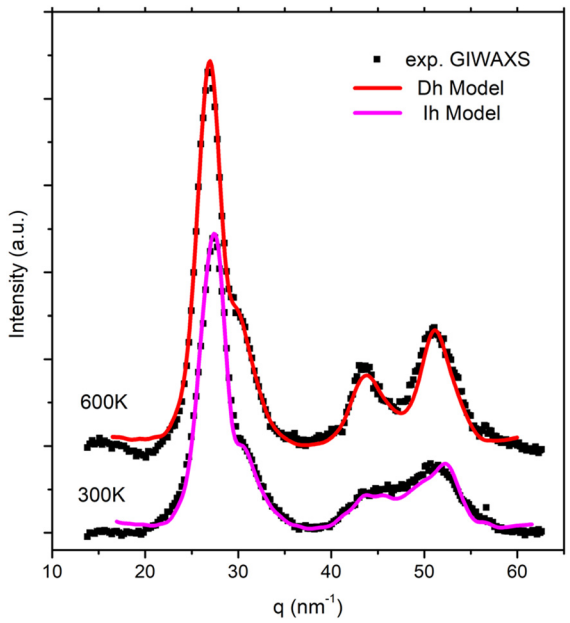

Fig. 7 GIWAXS experimental spectra obtained just after deposition at 300 K and after thermal activation at 600 K (dots); calculated spectra in good agreement with experiments are shown corresponding to a distribution of Ih structure models from Ag_{309} to Ag_{923} after energy minimization by MC simulation (magenta line) for the 300 K experimental spectrum and a mixed distribution of the Ih structure and Dh structure models from Ag_{318} to Ag_{967} (red line) for the 600 K experimental spectrum.

where E is the potential energy of the cluster, ε_b is the binding energy per atom in the bulk solid and N is the cluster size.[21] E_{exc} is calculated for the most relevant structural motifs (fcc, Ih and Dh), in the size range relevant to the experiments. For sizes around 147 atoms, Ih structures are the lowest in energy, and therefore they are expected to be dominant at equilibrium,

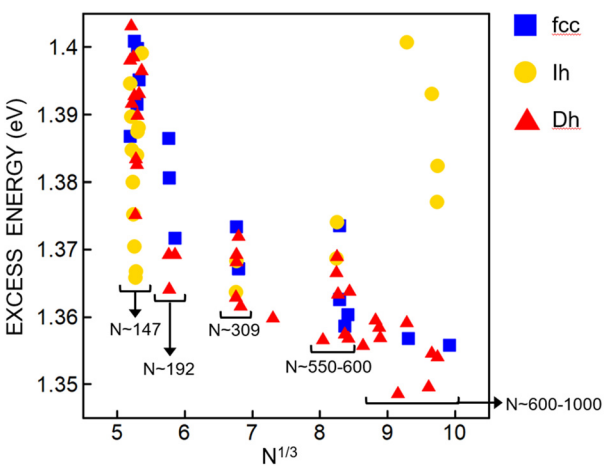

Fig. 8 Excess energy according to Gupta potental calculations, for different structural motifs in the size range relevant for the experiment (from $N \sim 147$ to $N \sim 1000$ atoms).

since entropic effects are known to further stabilize the Ih motif with an increase in temperature.[41,42] For sizes around 192 atoms, there is a competition between Dh and fcc structures, as a perfect Marks Dh and a perfect fcc truncated octahedron can be built for sizes 192 and 201, respectively. At $N \sim 309$ a rather close competition between all the three motifs is found. At larger sizes, Ih becomes highly unfavourable, even around the Ih magic sizes of 561 and 923 atoms. Dh structures dominate in this size range, with fcc truncated octahedra being quite favourable around the perfect size of 586 atoms. These results confirm that the experimental observation of Ih of sizes larger than 147 is likely to be due to non-equilibrium effects, and that equilibration obtained by ageing/annealing is likely to produce a majority of Dh structures. In order to check the stability of icosahedral structures we have performed annealing simulations at two different sizes (191 and 700 atoms) heated up to temperatures in the range 500–700 K. The results are reported in Fig. S4, and S5, ESI.† In both cases, the structures transform from Ih to Dh by complex rearrangement mechanisms of collective character. For size 191, the temperature dependence of the lifetime of the icosahedral structure well corresponds to an Arrhenius law in the range 500–600 K (see Fig. S5, ESI†), whose extrapolation to RT gives a lifetime of about 10 h, compatible with the experimental ageing times.

4. Discussion and conclusions

The experimental data identify continuous and regular growth within the icosahedral motif which persists in a size range where the Ih becomes metastable against Dh structures, which are shown to be more stable by ageing and annealing experiments. The simulations very well agree with the experimental findings, both for the growth outcomes and the analysis of energetic stability. In addition, the MD simulations show that smooth SBS growth, which preserves the icosahedral template with few defects, is possible down to RT even within their time scale, which is much shorter than that of experiments. The simulations give a clear picture of the underlying growth mechanisms at the atomic level. The typical growth pathway emerging from the simulations starts with the formation of faulted atomic islands, which are positioned on hcp (*i.e.* anti-Mackay) stacking. These islands are energetically favourable in the initial stage of shell formation, as also confirmed by the results of DFT calculations with three different exchange–correlation functionals. When the number of deposited atoms increases, the Mackay shell arrangement becomes energetically favourable instead. The anti-Mackay → Mackay transformation occurs at a glance by a collective displacement of many atoms, in some cases of all atoms in the top shell. These collective motions are not the most common diffusion events on the surface. In fact, the displacements of isolated adatoms are by far more frequent than the crucial collective events. The latter may occur only once before the completion of the shell, but, without them, growth would take a qualitatively different path. In our case, if anti-Mackay islands would persist, the

cluster would grow towards a different and much rougher shape. In order to investigate this point, we have simulated the growth on top of an icosahedron with an anti-Mackay outer shell whose atoms are kept fixed in order to suppress the aM → M transformation. The results are shown in Fig. S6, ESI.† A perfect smooth regular growth on top of such an anti-Mackay structure would lead to a pentakis-dodecahedral shape[43] instead of the experimentally observed Mackay icosahedron. However, grown structures are far from being smooth and regular even at 500 K because the fourfold adsorption sites between anti-Mackay islands act as adatom traps, which strongly slow down atomic mobility.

In the growth mechanism unveiled by our MD simulations, the inter-layer mobility of individual adatoms is not sufficient for achieving smooth and regular SBS growth. If several anti-Mackay islands are present, the rate-limiting process for SBS growth is not adatom descent from steps, as governed by the ES barrier, but the escape of adatoms from fourfold trapping sites between the islands. In reality, the picture is far more complex, as atoms do not escape from such sites, but the anti-Mackay islands transform into a Mackay cap so that all trapping sites are cleared, and growth can proceed smoothly, since interlayer mobility on Mackay caps is quite fast.

In summary, our results show that the growth path towards smooth icosahedra is decided by a few rare *black swan* collective events. Our findings are representative of the kinetics of pure silver clusters growing in the solid state and, as such, they reveal mechanisms that are likely common to other metallic nanoparticles growing under the same conditions. Indications in this sense come from the analysis of other experiments and simulations concerning the growth and evolution of different metallic clusters and nanoparticles.[7,8,44–46] If the growth procedure involves ligands that may change the diffusion kinetics of the atoms on the nanoparticle surface, other mechanisms might be activated. On the other hand, if growth takes place in the liquid phase and then metal droplets solidify after the completion of growth, as in this case the formation processes may be quite different.

Author contributions

D. N. performed and analysed the growth simulations. C. R. performed the DFT calculations. R. F. performed and analyzed the annealing simulations. P. A., C. A.-V. and Z. K. developed the growth and annealing method. P. A., Z. K., A. C. and Y. G. performed the *in situ* synchrotron radiation measurements and C. A. performed the HRTEM observations. P. A. performed the scattering spectra simulations and experimental data analysis. All authors contributed to writing the paper.

Conflicts of interest

There are no conflicts to declare.

Acknowledgements

The authors would like to acknowledge support from the International Research Network – IRN Nanoalloys of CNRS. D. N., C. R. and R. F. acknowledge support from the PRIN 2017 project UTFROM of the Italian MIUR, from the Progetto di Eccellenza of the Physics Department of the University of Genoa, and from the IRN Nanoalloys of CNRS. The Z. K., Y. G., A. C., C. A.-V. and P. A. acknowledge the SOLEIL (Gif sur Yvette, France) synchrotron facility for synchrotron radiation access and the SixS beamline team, especially Benjamin Voisin for technical help. The authors are grateful to Daniel Förster for helpful discussions. This project has benefited from the facilities (JEOL ACCELARM 200) of UAR MACLE-CVL which was co-funded by the European Union (FEDER) and the Centre-Val de Loire Region.

References

1 H. Brune, *Surf. Sci. Rep.*, 1998, **31**, 125–229.
2 X. Wang, S. Zheng, S. Shinzato, Z. Fang, Y. He, L. Zhong, C. Wang, S. Ogata and S. X. Mao, *Nat. Commun.*, 2021, **12**, 5237.
3 P. Z. Chen, A. Skirzynska, T. Yuan, O. Voznyy and F. X. Gu, *J. Am. Chem. Soc.*, 2022, **144**, 19417–19429.
4 W. Dachraoui, M. I. Bodnarchuk and R. Erni, *ACS Nano*, 2022, **16**, 14198–14209.
5 W. Dachraoui, M. I. Bodnarchuk, A. Vogel, M. V. Kovalenko and R. Erni, *Appl. Phys. Rev.*, 2021, **8**, 041407.
6 K. A. Fichthorn and T. Yan, *J. Phys. Chem. C*, 2021, **125**, 3668–3679.
7 Y. Xia, D. Nelli, R. Ferrando, J. Yuan and Z. Y. Li, *Nat. Commun.*, 2021, **12**, 3019.
8 E. y. El koraychy, C. Roncaglia, D. Nelli, M. Cerbelaud and R. Ferrando, *Nanoscale Horiz.*, 2022, **7**, 883–889.
9 S. F. Tan, S. W. Chee, G. Lin, M. Bosman, M. Lin, U. Mirsaidov and C. A. Nijhuis, *J. Am. Chem. Soc.*, 2016, **138**, 5190–5193.
10 N. Ahmad, M. Bon, D. Passerone and R. Erni, *ACS Nano*, 2019, **13**, 13333–13342.
11 W. Gao, A. O. Elnabawy, Z. D. Hood, Y. Shi, X. Wang, L. T. Roling, X. Pan, M. Mavrikakis, Y. Xia and M. Chi, *Nat. Commun.*, 2021, **12**, 3215.
12 J. Wu, W. Gao, J. Wen, D. J. Miller, P. Lu, J.-M. Zuo and H. Yang, *Nano Lett.*, 2015, **15**, 2711–2715.
13 Q. Zhang, J. Xie, J. Yang and J. Y. Lee, *ACS Nano*, 2009, **3**, 139–148.
14 H. Wang, S. Zhou, K. D. Gilroy, Z. Cai and Y. Xia, *Nano Today*, 2017, **15**, 121–144.
15 A. Pimpinelli and J. Villain, *Physics of Crystal Growth*, Cambridge University Press, 1998.
16 T. Ala-Nissila, R. Ferrando and S. C. Ying, *Adv. Phys.*, 2002, **51**, 949–1078.
17 K. C. Lai, Y. Han, P. Spurgeon, W. Huang, P. A. Thiel, D.-J. Liu and J. W. Evans, *Chem. Rev.*, 2019, **119**, 6670–6768.

18 G. Ehrlich and F. Hudda, *J. Chem. Phys.*, 1966, **44**, 1039–1049.
19 R. L. Schwoebel, *J. Appl. Phys.*, 1968, **40**, 614–618.
20 D. Nelli, C. Roncaglia and C. Minnai, *Adv. Phys.: X*, 2023, **8**, 2127330.
21 F. Baletto and R. Ferrando, *Rev. Mod. Phys.*, 2005, **77**, 371–423.
22 J. Penuelas, C. Andreazza-Vignolle, P. Andreazza, A. Ouerghi and N. Bouet, *Surf. Sci.*, 2008, 545–551.
23 P. Andreazza, C. Mottet, C. Andreazza-Vignolle, J. Penuelas, H. Tolentino, M. D. Santis, R. Felici and N. Bouet, *Phys. Rev. B: Condens. Matter Mater. Phys.*, 2010, **82**, 155453.
24 J. Penuelas, P. Andreazza, C. Andreazza-Vignolle, H. Tolentino, M. D. Santis and C. Mottet, *Phys. Rev. Lett.*, 2008, **100**, 115502.
25 P. Andreazza, Probing Nanoalloy Structure and Morphology by X-Ray Scattering Methods, in *Nanoalloys – Synthesis, Structure and Properties*, D. Alloyeau, C. Mottet and C. Ricolleau, Springer Verlag, Berlin, 2012, pp. 69–112.
26 J. Barthel, *Ultramicroscopy*, 2018, **193**, 1–11.
27 A. Coati, L. M. G. Chavas, P. Fontaine, N. Foos, B. Guimaraes, P. Gourhant, P. Legrand, J.-P. Itie, P. Fertey, W. Shepard, T. Isabet, S. Sirigu, P.-L. Solari, D. Thiaudiere and A. Thompson, *Eur. Phys. J. Plus*, 2017, **132**, 174.
28 P. Andreazza, A. Lemoine, A. Coati, D. Nelli, R. Ferrando, Y. Garreau, J. Creuze and C. Andreazza-Vignolle, *Nanoscale*, 2021, **13**, 6096–6104.
29 L. Virot and P. Andreazza, *XDSS Software*, Orléans, France, 2006.
30 P. Giannozzi, S. Baroni, N. Bonini, M. Calandra, R. Car, C. Cavazzoni, D. Ceresoli, G. L. Chiarotti, M. Cococcioni, I. Dabo, A. D. Corso, S. de Gironcoli, S. Fabris, G. Fratesi, R. Gebauer, U. Gerstmann, C. Gougoussis, A. Kokalj, M. Lazzeri, L. Martin-Samos, N. Marzari, F. Mauri, R. Mazzarello, S. Paolini, A. Pasquarello, L. Paulatto, C. Sbraccia, S. Scandolo, G. Sclauzero, A. P. Seitsonen, A. Smogunov, P. Umari and R. M. Wentzcovitch, *J. Phys.: Condens. Matter*, 2009, **21**, 395502.
31 J. P. Perdew, K. Burke and M. Ernzerhof, *Phys. Rev. Lett.*, 1996, **77**, 3865–3868.
32 J. P. Perdew, A. Ruzsinszky, G. I. Csonka, O. A. Vydrov, G. E. Scuseria, L. A. Constantin, X. Zhou and K. Burke, *Phys. Rev. Lett.*, 2008, **100**, 136406.
33 R. Parr and W. Yang, *Density-Functional Theory of Atoms and Molecules*, Oxford University Press, 1994.
34 M. Zinke-Allmang, L. C. Feldman and M. H. Grabow, *Surf. Sci. Rep.*, 1992, **16**, 377–463.
35 J. Penuelas, P. Andreazza, C. Andreazza-Vignolle, C. Mottet, M. De Santis and H. C. N. Tolentino, *Eur. Phys. J.: Spec. Top.*, 2009, **167**, 19–25.
36 A. Hizi, G. D. Forster, R. Ferrando, Y. Garreau, A. Coati, C. Andreazza-Vignolle and P. Andreazza, *Faraday Discuss.*, 2023, **242**, 35–51.
37 R. Ferrando and G. Tréglia, *Surf. Sci.*, 1997, **377–379**, 843–846.
38 D. Bochicchio and R. Ferrando, *Nano Lett.*, 2010, **10**, 4211–4216.
39 F. Baletto and R. Ferrando, *Surf. Sci.*, 2001, **490**, 361.
40 D. Loffreda, D. M. Foster, R. E. Palmer and N. Tarrat, *J. Phys. Chem. Lett.*, 2021, **12**, 3705–3711.
41 J. P. K. Doye and F. Calvo, *Phys. Rev. Lett.*, 2001, **86**, 3570–3573.
42 D. Nelli, C. Roncaglia, R. Ferrando and C. Minnai, *J. Phys. Chem. Lett.*, 2021, **12**, 4609–4615.
43 K. Laasonen, E. Panizon, D. Bochicchio and R. Ferrando, *J. Phys. Chem. C*, 2013, **117**, 26405–26413.
44 F. Baletto, *J. Phys.: Condens. Matter*, 2019, **31**, 113001.
45 K. A. Fichthorn, *Chem. Rev.*, 2023, **123**, 4146–4183.
46 P. N. Plessow, *Phys. Chem. Chem. Phys.*, 2020, **22**, 12939–12945.